Supplementary Information

Hydrogen-Directed Au–H–Au Chain Networks Redefine the Active Structure of Sub-2 nm Gold Nanoparticles

Loréna Chabeaud[1]

Nicolás F. Barrera[2], Julia Contreras-García[2], Julien Lam[3] and Hazar Guesmi[1*]

[1] ICGM, UMR 5253, Univ Montpellier, CNRS, ENSCM, Montpellier, France

[2] Laboratoire de Chimie Théorique, Sorbonne Université and CNRS, 4 Pl Jussieu, F-75005, Paris, France

[3] Université Lille, Centre National de la Recherche Scientifique, INRA, ENSCL, UMR 8207, UMET, Unité Matériaux et Transformations, 59000 Lille, France

AUTHOR INFORMATION

hazar.guesmi@umontpellier.fr

I. Computational details

Energetic analysis

To quantify H induced geometry restructuration, we computed radial distribution functions g(r) and bond angle distributions for Au–Au pairs. Coordination numbers (CN) were determined by a cutoff r_{cut} = 3.5 Å including only nearest neighbors. The energetic analysis was carried out to disentangle the individual contributions of deformation and interaction effects. The following energetic quantities were defined:

- The normalized cohesion energy E_{coh} (eV·atom^{-1}) was calculated as:

$$E_{coh} = \frac{E_{NP}^{opt} - N_{Au}.E_{at}}{N_{Au}} \# \quad \#Eq.\ 1$$

Where E_{NP}^{opt} is the total electronic energy of the Au NP (Ico or TOh), E_{at} (eV) is the total electronic energy of an isolated Au atom in its doublet ground state, and N_{Au} is the number of Au atoms in the NP (N = 147 for Ico and N = 201 for TOh).

- The excess energy per surface Au atom, E_{exc}(eV) normalized by the number of surface atoms (122 for TOh and 92 for Ico) was determined as:

$$E_{exc} = \frac{E_{NP}^{opt} - N_{Au}.E_{bulk}^{FCC}}{N_{surf}} \# \#Eq.\ 2$$

Where E_{bulk}^{FCC} is the total electronic energy per atom of bulk fcc Au and N_{surf} is the number of surface atoms in the NP ($N_{surf} = 92$ for Ico and $N_{surf} = 122$ for TOh). E_{exc} measures the energetic penalty per surface atom relative to bulk; lower values denote higher thermodynamic stability (at fixed size and composition) and enable a direct comparison between TOh and Ico morphologies.

- Interaction energies for the adsorption of hydrogen on Au NP were computed according to Eq. 3:

$$E_{int} = \frac{E_{NP+nH^{ads}} - \left(E_{NP}^{*} + n.E_{H}^{gas}\right)}{n} \#Eq.\ 3$$

Here, $E_{NP+nH^{ads}}$ is the total electronic energy of the hydrogen covered NP and E_{NP}^{*} is the single point energy of the clean NP evaluated at the geometry obtained by removing all adsorbates from the optimized hydrogenated structure (no further relaxation). E_{H}^{gas} is the energy of an isolated gas phase H atom, taken as one half of the total energy of H_2 in the gas phase and corrected by one half of the experimental H_2 dissociation energy (4.75 eV) [1]. By this convention, negative E_{int} denotes exothermic interaction.

- The adsorption energy, E_{ads}, is defined by:

$$E_{ads} = \frac{E_{NP+nH^{ads}} - \left(E_{NP}^{opt} + n.E_{H}^{gas}\right)}{n} \#Eq.\ 4$$

Negative E_{ads} denotes exothermic, stabilizing Au–H adsorption. Let us note that E_{ads} includes both the Au–H interaction and the deformation penalty E_{def}^{NP} required to distort the NP from its relaxed structure to the adsorption geometry. In practice, E_{int} is typically more negative than E_{ads}; their difference cleanly measures how much structural distortion of the NP is "paid" to enable adsorption. This deformation penalty, hereafter referred to as E_{def}, is defined in Eq. 5 as:

$$E_{def} = \left(E_{ads} - E_{int}\right).\frac{n}{N_{Au}} \#Eq.\ 5$$

Electronic structure analysis

Density of states

Self-consistent charge densities were computed on fine FFT grids to ensure consistent real space sampling for all models. Total and projected densities of states (DOS/PDOS) were analyzed, and the Au d-band center was evaluated relative to the Fermi level as:

$$\varepsilon_d = \frac{\int_{-\infty}^{E_F} \varepsilon n_d(\varepsilon) d\varepsilon}{\int_{-\infty}^{E_F} n_d(\varepsilon) d\varepsilon} - E_F \#Eq.\ 6$$

Where $\varepsilon n_d(\varepsilon)$ is the d-projected DOS (integrals over the occupied states). Local charge distributions were evaluated by Bader charge analyses using the Henkelman code [2]. As cluster calculations involve large vacuum regions, special care was taken in the charge partitioning to avoid spurious vacuum basins.

Charge density

Charge-density difference was computed and mapped according to the equation 7:

$$\Delta\rho(r) = \rho_{NP+nH}(r) - \left(\rho_{NP}(r) + \sum_{i=1}^{n} \rho_H^{isol}(r - R_i)\right) \#Eq.\ 7$$

Where $\rho_{NP+nH}(r)$ is the self-consistent electron density of the hydrogenated NP, $\rho_{NP}(r)$ is the density of the corresponding clean NP and ρ_H^{isol} denotes the density of an isolated H atom; the latter term is the non-interacting superposition of n such densities placed at the adsorption sites R_i. All densities were evaluated in the same simulation cell, with identical numerical settings, at the adsorption geometries.

Electron Localization analysis

Electron localization was examined using the Electron Localization Function (ELF) [3, 4]. ELF probes the excess local kinetic energy density arising from Pauli repulsion and typically exhibits maxima in regions where electrons are localized, consistent with the Lewis picture. ELF values at saddle points can then be used to quantify the degree of delocalization between electron pairs [5].

The network of ELF maxima and saddle points was determined using the CRITIC2 code [6]. In addition, weak interactions present in the nanostructures were also analyzed using the NCI index [7] as implemented in the NCIPLOT software [8, 9]. NCI enables visualization of non-covalent interactions as isosurfaces between atoms, typically colored according to the interaction type: blue for strong attractive interactions (e.g., hydrogen bonding), green for van der Waals interactions, and red for steric repulsion.

Fukui function analysis

We use Fukui functions [10] as frontier reactivity descriptors to identify regions that are intrinsically more prone to electrophilic attack (i.e., regions that donate charge to an electrophile) or nucleophilic attack (i.e., regions that accept charge from a nucleophile) and to rank potential adsorption/activation sites, disregarding electrostatic interactions. The Fukui function is the derivative of the electron density with respect to the electron number (N_e) at fixed external potential v(r) as expressed by Eq. 8.

$$f(r) = \left(\frac{\partial\rho(r)}{\partial N_e}\right)_v \#\ \#Eq.\ 8$$

Since the total energy is piece wise linear with respect to the electron number and exhibits a derivative discontinuity at integer N_e, the Fukui functions are evaluated using the standard finite-difference definitions, i.e., $f^+(r) = \rho_{N_e+1}(r) - \rho_{N_e}(r)$ for electron addition and $f^-(r) = \rho_{N_e}(r) - \rho_{Ne-1}(r)$ for electron removal. In doing so, we neglect the effects of the compensating background charge on the Fukui functions [11].

II. Results and discussion

Surface-restricted RDFs for Au–Au and Au–H pairs (Fig. SI.1)

To quantify the hydrogen-induced restructuring of the outer shell, surface-restricted RDFs g(r) is reported in Figure SI.1 for Au–Au (top row) and Au–H (bottom row) pairs, comparing the Ico (left column) and TOh (right column) NPs across Models I–III.

In the fixed-lattice reference (Model I), the surface Au–Au first-neighbor peak is centered at ∼2.91 Å for the Ico and at ∼2.85 Å for the TOh, (Fig. SI.1a–b) bracketing the bulk Au nearest-neighbor distance (2.88 Å) and reflecting the well-known distinct intrinsic surface strain/relaxation of the two motifs [12-13]. Upon full relaxation under hydrogen (Model II), the surface Au–Au distribution collapses toward shorter distances, with a dominant first-shell peak near ∼2.79 Å for both morphologies and a strong attenuation of medium-range order, consistent with local surface reconstructions and the emergence of bridged Au–H–Au motifs that draw near-surface Au atoms together. After finite-temperature sampling at 300 K followed by 0 K relaxation (Model III), the surface compaction is further reinforced. The first-neighbor surface peak shifts to ∼2.73 Å in both NPs, remaining significantly shorter than bulk Au and indicating that thermally assisted restructuring stabilizes contracted Au–Au bonds within the hydrogenated surface network.

The corresponding surface Au–H distributions (Fig. SI.1c–d) display a first-shell peak consistently located near ∼1.77 Å across Models I–III and across both morphologies. Importantly, this Au–H peak narrows from Model I to Model III, indicating an increasingly uniform H environment as the surface reorganizes into predominantly bridging geometries along Au–H–Au chains. A minor population of hydrogen atoms remains bound at apical or

terminal Au-chain sites, with Au–H bond lengths ranging in the 1.58–1.63 Å range, reflecting residual local heterogeneity at the reconstructed surface.

Overall, the surface-restricted RDFs show that hydrogen compacts near-surface Au–Au bonds while preserving a nearly invariant Au–H first-shell distance, thereby stabilizing a contracted, chain-rich active surface ensemble.

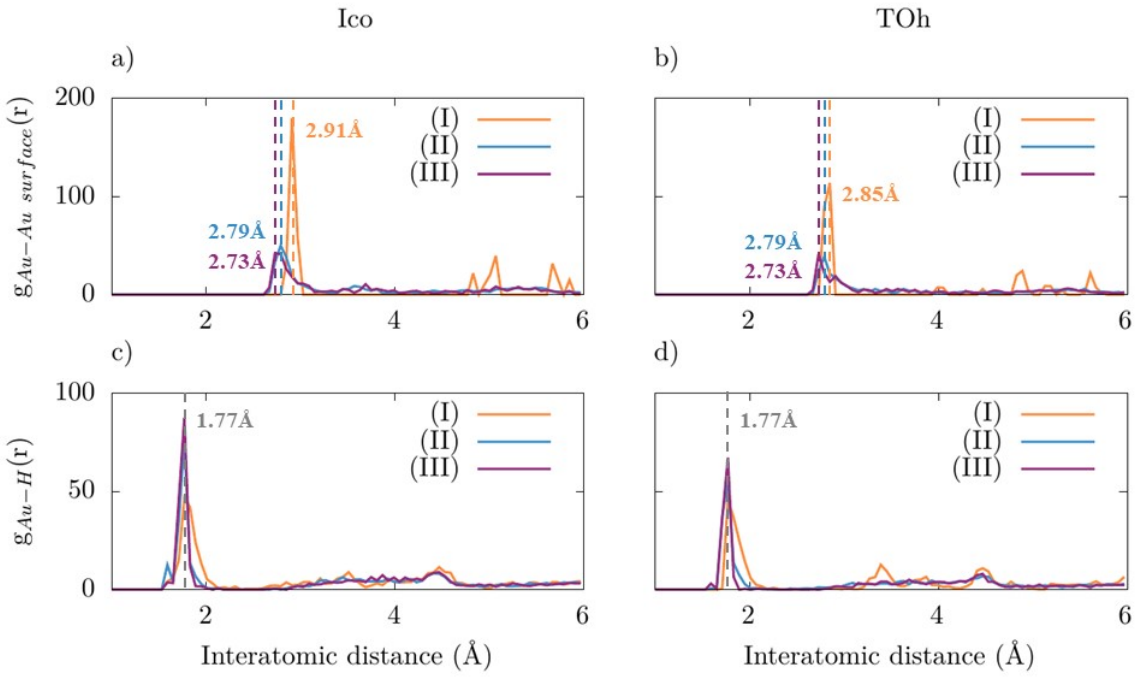

Figure SI.1: *Surface-restricted radial distribution functions g(r) for (a–b) Au–Au and (c–d) Au–H pairs in hydrogenated sub-2 nm Au NPs. Left column: Ico; right column: TOh NPs. Curves compare Model I (frozen-lattice adsorption), Model II (fully relaxed at 0 K), and Model III (structures sampled at 300 K by AIMD and subsequently relaxed at 0 K). Distributions are computed using surface atoms only.*

Core (bulk-like) Au–Au RDFs (Fig. SI.2): The core-restricted Au–Au radial distribution functions highlight that hydrogen-driven restructuring remains primarily a surface phenomenon while inducing a measurable, but secondary, strain response in the interior. In the frozen-lattice references (Model I), the truncated octahedron displays the expected fcc-like nearest-neighbor signature, with a short-distance component near ~2.79 Å (in-plane spacing within close-packed layers) and a longer-distance feature near ~2.97 Å (interlayer separation). In contrast, the icosahedral core exhibits an "inverted" assignment: the alternating fcc/hcp stacking intrinsic to Mackay icosahedra compresses inter-shell contacts toward ~2.79 Å while expanding intra-shell distances toward ~2.91 Å, reflecting the well-known internal strain associated with fivefold symmetry [12, 13]. Upon full relaxation under hydrogen (Model II), both morphologies

converge toward a more bulk-like first-neighbor peak near ~2.85 Å and the medium-range order becomes attenuated, indicating partial strain redistribution and increased static disorder transmitted from the reconstructed surface. After 300 K sampling and quench (Model III), the truncated octahedron core shifts back toward ~2.79 Å (more fcc-like packing recovery), whereas the icosahedral core remains centered near ~2.85 Å, consistent with residual internal strain and the persistence of a slightly dilated/disordered interior even as the surface becomes strongly compacted.

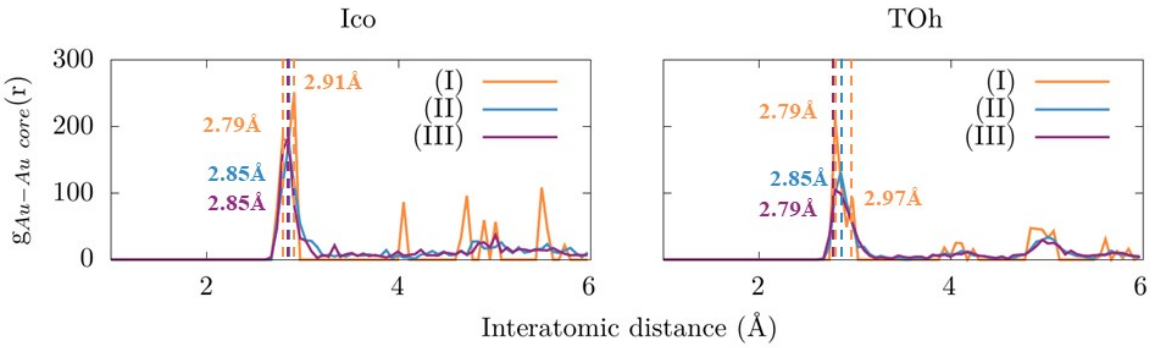

Figure SI.2: *Core restricted Au–Au radial distribution functions g(r) for icosahedral (left) and truncated octahedral (right) Au NPs across Models I–III. Distributions are computed using core atoms only and complement the surface restricted RDFs shown in Figure SI.1.*

Dynamic low-coordination number of Au surface (Fig. SI.3a, SI.3b and movie M1): Coordination numbers (CN) were evaluated from Au–Au pairs using a cutoff r_{cut} = 3.5 Å, which encloses the entire first-neighbor shell for all structures considered (cf. the first-shell maxima at ~2.73–2.97 Å (Fig. SI.1). CN are classified and mapped to geometric motifs as follows: < 6 (vertices/chain atoms), 7 (edges), 8 (100) facets, 9 (111) facets, 10–11 (sub-surface), 12 (fcc-like bulk).

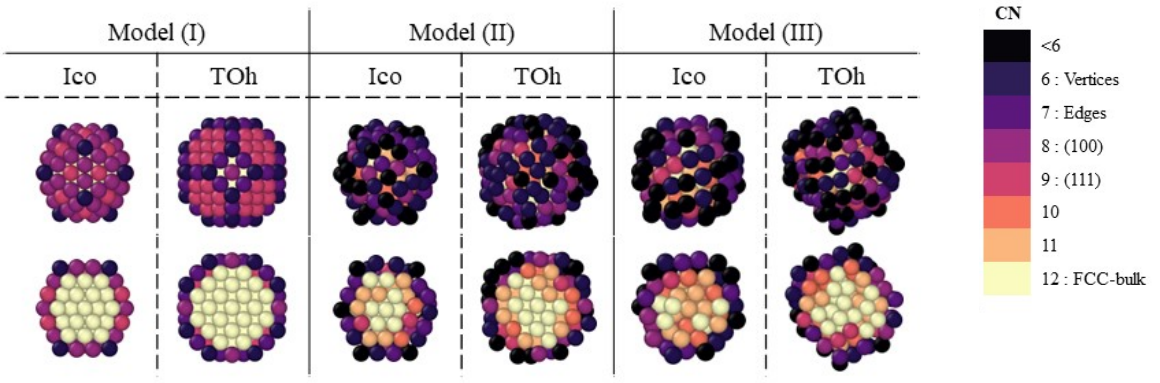

Figure SI.3a: ***Coordination-number (CN) of surface Au NPs.*** *Color-coded CN maps for Ico and TOh NPs across Models I–III (H removed for clarity).*

Fig. SI.3b provides a pictorial complement to the time-dependent coordination-number (TDCN) analysis discussed in the main text (Fig. 1.d). Over the last 7 ps of the 300 K AIMD trajectory (27–34 ps), Au atoms belonging to representative surface Au–H–Au–H chains exhibit pronounced yet reversible changes in their local coordination environments. The instantaneous CN values (restricted to CN ≤ 7 and evaluated using the same CN definition as in the main text) fluctuate frequently between adjacent integers, highlighting the fluxional character of surface Au–Au bonding and the continuous exchange of bonds with near-subsurface atoms. The schematic sequence in Fig. SI.3.b was assembled from representative frames extracted from Movie M1, spanning the same 7 ps time window.

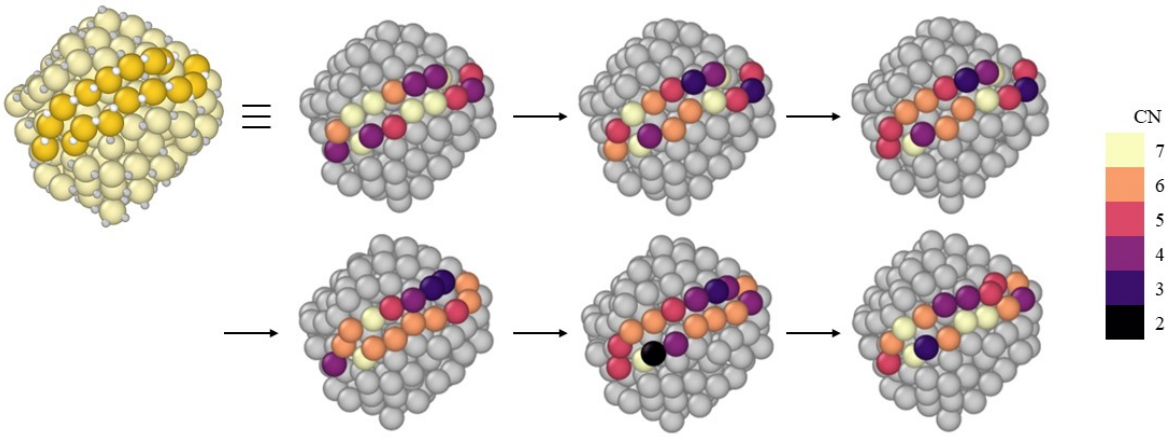

Figure SI.3b: *Snapshot sequence illustrating reversible coordination-number (CN) fluctuations in a surface Au–H–Au–H chain during AIMD at 300 K. Left, the model system is shown with the subset of near-surface Au atoms involved in the chain highlighted. Right, a close-up sequence of representative snapshots extracted from Movie M1 over the last 7 ps of the trajectory (27–34 ps; same time window as Fig. 1.d) illustrates the pronounced yet reversible coordination changes of the chain Au atoms. Chain Au atoms are colored according to their instantaneous CN (CN ≤ 7; color bar), evidencing frequent transitions between adjacent CN values associated with Au–Au surface fluxionality and bond exchange with near-subsurface atoms; all other Au atoms are shown in grey. Arrows indicate chronological progression.*

Energetic driving forces: Au–H stabilization versus metal deformation (Table SI.1)

Table SI.1 summarizes the energetics of pristine and hydrogenated Au NPs. For the pristine NPs, the TOh morphology is found to be slightly more stable than the Ico one with E_{coh} = −3.14 eV.atom^{-1} vs −3.06 eV.atom^{-1} (TOh vs Ico) and E_{exc} = 0.91 eV vs 1.01 eV per surface atom. These two computed values are consistent because they quantify stability from complementary angles. The E_{coh} measures the average binding strength (more negative energy means more strongly bound), whereas the E_{exc} measures the surface energy penalty relative to bulk (smaller energy means closer to the bulk limit). This result showing lower-energy TOh framework before hydrogen adsorption aligns with the established size-dependent competition between non-crystalline motifs (icosahedral/decahedral) and fcc-derived Wulff shapes in late-metal clusters. Indeed, at the smallest sizes, Ico structures can be competitive, or even be preferred, because they minimize surface energy on close-packed (111) facets. However, with increasing size, the build-up of elastic strain associated with fivefold symmetry penalizes icosahedra, and fcc morphologies (cuboctahedra/TOh) become favored, a difference that increases as NP size grows [14].

Table 1: *Energetics of pristine NPs (Model 0), hydrogen adsorption (Model I) and adsorption-induced deformation in sub-2 nm gold NPs with Ico and TOh geometries (Models II–III). E_{coh}, E_{exc} and E_{def} are reported per Au atom, whereas E_{int} and E_{ads} are reported per H.*

		E_{coh} (eV/Au)	E_{exc} (eV/Au_{surf})	E_{ads} (eV/H)	E_{int} (eV/H)	E_{def} (eV/Au)
TOh	Au_{201} (0)	-3.14	0.91			
	$Au_{201}H_{122}$ (I)			-2.10	-2.10	
	$Au_{201}H_{122}$ (II)			-2.22	-2.45	0.14
	$Au_{201}H_{116}$ (III)			-2.25	-2.53	0.16
Ico	Au_{147} (0)	-3.06	1.01			
	$Au_{147}H_{92}$ (I)			-2.12	-2.12	
	$Au_{147}H_{92}$ (II)			-2.24	-2.42	0.11
	$Au_{147}H_{80}$ (III)			-2.30	-2.55	0.13

Upon hydrogen adsorption and subsequent structural relaxation, the intrinsic Au–H interaction energy E_{int} is strongly stabilized. This value evolves from −2.10 to −2.45 and −2.53 eV/H for TOh, and from −2.12 to −2.42 and −2.55 eV/H for Ico, yielding an identical net gain of −0.43 eV/H for both morphologies. This stabilization is partially offset by the deformation penalty of the Au framework, quantified by deformation energy E_{def} (0.14–0.16 eV/Au for TOh and 0.11–0.13 eV/Au for Ico).

Au-Au ELF connectivity from topological analysis (Fig. SI.4): Figure 2d in the main text plots the values of the highest ELF isovalue at which the two basins remain connected as a function of the radial distance from the NP center. Representative ELF isosurfaces at ELF = 0.25 are depicted in Figure SI.4. The results visually confirm that the reconstructed structure retains an electronically connected surface network up to higher ELF levels.

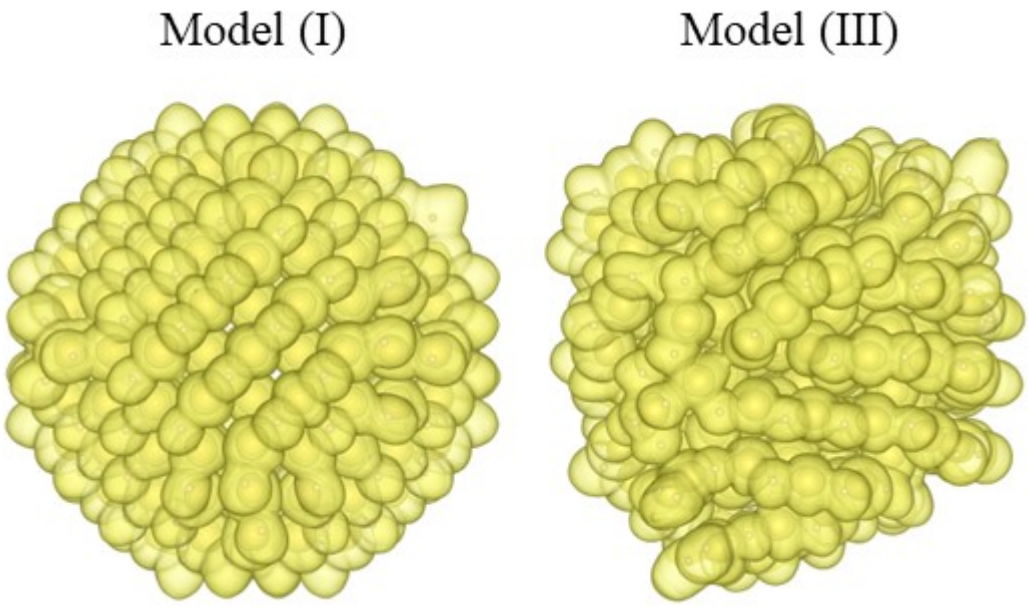

Figure SI.4: *Au–Au ELF connectivity derived from topological analysis. Representative ELF isosurfaces at ELF = 0.25 are shown for Model I (left) and Model III (right). The persistence of a continuous Au–Au isosurface in Model III demonstrates that, despite hydrogen-driven reconstruction, the near-surface region remains electronically connected at this localization threshold.*

NCI: weak, mostly dispersive contacts between neighboring chain segments (Fig. SI.5): NCI analysis (NCIPLOT) was used to qualitatively characterize low-density contacts between neighboring Au–H–Au chain segments. Reduced density gradient isosurfaces are predominantly green, indicating mainly weak dispersive interactions. In Model III, only localized attractive regions appear at a few crowded junctions where chain segments approach closely, while no extended attractive surfaces connect entire segments. This supports that the chain network is not rigidly "glued" by strong directional inter-segment interactions; cohesion is mainly associated with the Au–H–Au bridging framework and the reconstructed compact surface.

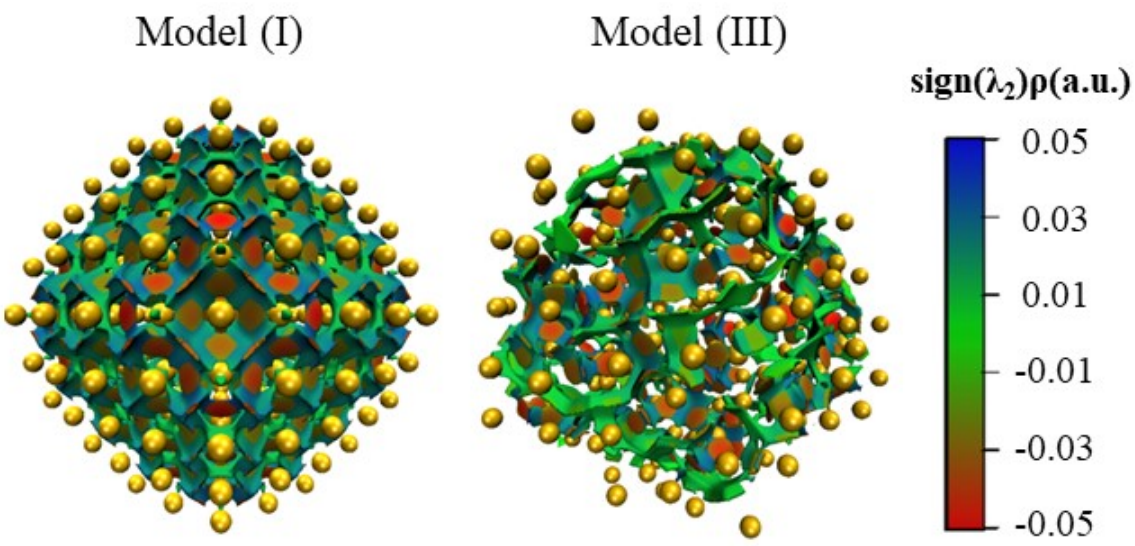

Figure SI.5: *NCI isosurfaces computed with NCIPLOT showing non covalent interactions in Model III between the core and the surface. We can see that van der Waals dominates, but some strong interactions (dark blue) are also present towards the surface.*

Charge-density redistribution, weakened metallic bonding and chain directionality (Fig. SI.6): Hydrogen-induced restructuring is accompanied by a pronounced reorganization of the electronic density, which explains both why the surface reconstructs and why it does so in the form of chains. The charge-density differences $\Delta\rho(r)$ (Eq. 7) between the hydrogenated NP and the superposition of the clean NP and isolated H atoms (Fig. SI.6) reveal a net charge transfer from surface Au to adsorbed hydrogen. Yellow lobes on adsorbed H indicate charge accumulation, while blue lobes on the outer Au layer indicate electron depletion, i.e. a positively polarized Au surface and partial hydride character of H.

In Model I, depletion extends beyond the Au–H bonds into Au–Au bonding regions within the outermost layer and between surface and subsurface atoms. Such depletion corresponds to weakened metallic bonding both in-plane and vertically, making the outer shell mechanically softer and more prone to reconstruction. Once the Au lattice is allowed to relax (Model III), the same net Au-H transfer is preserved but becomes oriented along the extended Au–H–Au chains. Furthermore, the core remains essentially unaffected in both models, in line with radial-distribution analysis.

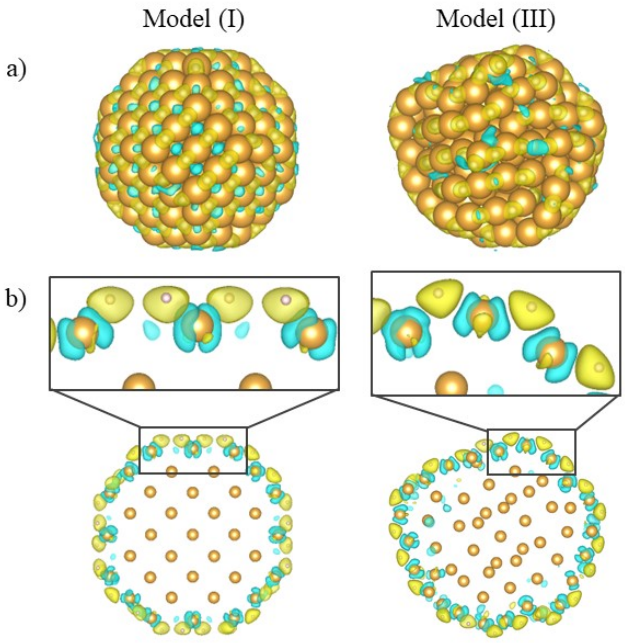

Figure SI.6: *Charge-density differences Δρ(r) between the hydrogenated NP and the superposition of the bare NP and isolated H atoms. (a) Global view at an isovalue of 0.002 e.bohr^{-3}; (b) Cross section of the NP along the z axis at 0.005 e.bohr^{-3} with a zoom on a representative Au–H. Yellow and blue isosurfaces indicate charge accumulation and depletion, respectively.*

Density of state analysis (Figs. SI.7, SI.8 and SI.9)

TDOS of pristine and H-covered nanoparticles (Fig. SI.7): Figure SI.7 compares the total density of states (TDOS) of the pristine icosahedral (Ico) and truncated-octahedral (TOh) Au NPs with their hydrogen-covered counterparts (Models I–III). The pristine clusters exhibit sharp, highly structured spectral features, consistent with finite-size level quantization and high structural symmetry. Upon H adsorption (with or without subsequent relaxation/reconstruction), the TDOS becomes markedly smoother and broader, reflecting symmetry breaking and the emergence of a wider distribution of local Au environments (splitting/broadening of discrete levels). In addition, a reproducible deep-valence shoulder/peak develops around ~−8.5 eV as soon as H is adsorbed. Based on the H- and Au-projected DOS (Fig. SI.8), this feature is assigned to Au(5d)–H(1s) hybridization. Despite these changes, the TDOS retains finite spectral weight at the Fermi level, consistent with preservation of an overall metallic electronic structure.

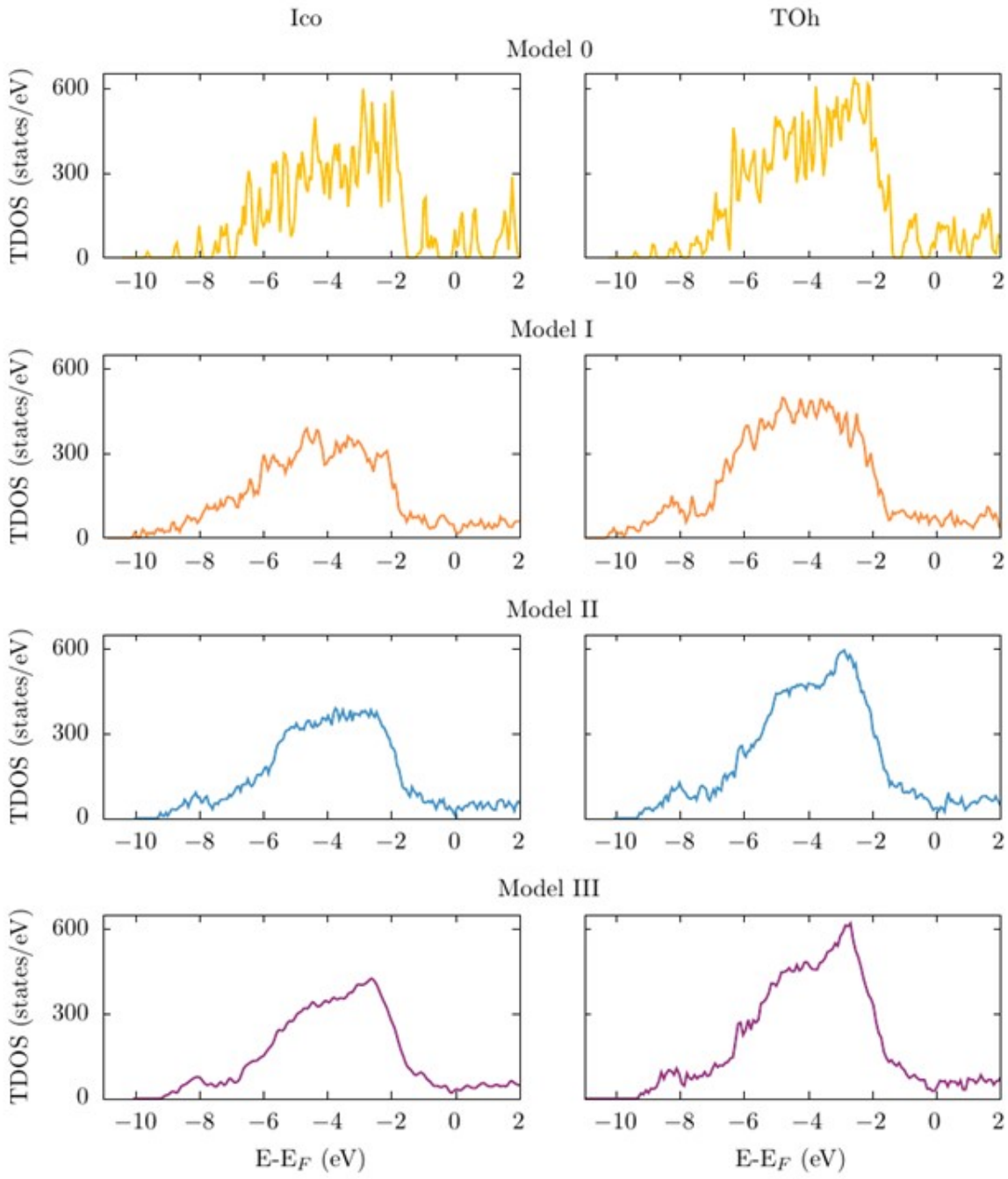

Figure SI.7: *Total density of states (TDOS) for icosahedral (Ico, left) and truncated-octahedral (TOh, right) Au NPs in the pristine state and under hydrogen coverage (Models I–III).*

Orbital-resolved projected density of states (PDOS) comparison for H adsorption on Au surface atoms in perfect and reconstructed nanoparticles (Fig. SI.8): Figure SI.8 compares orbital-resolved projected density of states (PDOS) for a representative Au surface atom and the H adsorbate bound to it, with energies referenced to E_F. Left panel depicts an edge Au atom

in the pristine TOh NP (Model I) with a hydrogen adsorbate bound at a bridge site, whereas right panel shows a chain-site Au atom in the reconstructed structure (Model III) with hydrogen adsorbed at the corresponding bridge position. In both cases, the Au PDOS is dominated by the 5d manifold in the [−6; −2] eV range, whereas finite spectral weight at E_F is retained and primarily associated with delocalized Au 6s/6p character. The H PDOS exhibits sharp features in the deep-valence region, evidencing Au–H hybridization. For the bridging edge configuration, a dominant narrow H-derived peak appears around ∼−8.5 eV, overlapping with the low-energy tail of Au(d) states. In the chain environment, the H-derived signal becomes more structured and redistributes toward higher energies, with pronounced weight appearing closer to the top of the Au d-band (notably around ∼−6 eV), consistent with a modified, more multicenter Au–H–Au interaction along the reconstructed network. The limited H weight near E_F supports a picture in which Au–H–Au motifs remain embedded in a delocalized metallic framework rather than forming molecular-like AuH fragments.

The Figure SI.8 also shows how reconstruction compresses and upshifts the Au 5d manifold, moving the d-band center from $\varepsilon_d = -3.685$ eV to −3.298 eV ($\Delta\varepsilon_d \approx +0.40$ eV).

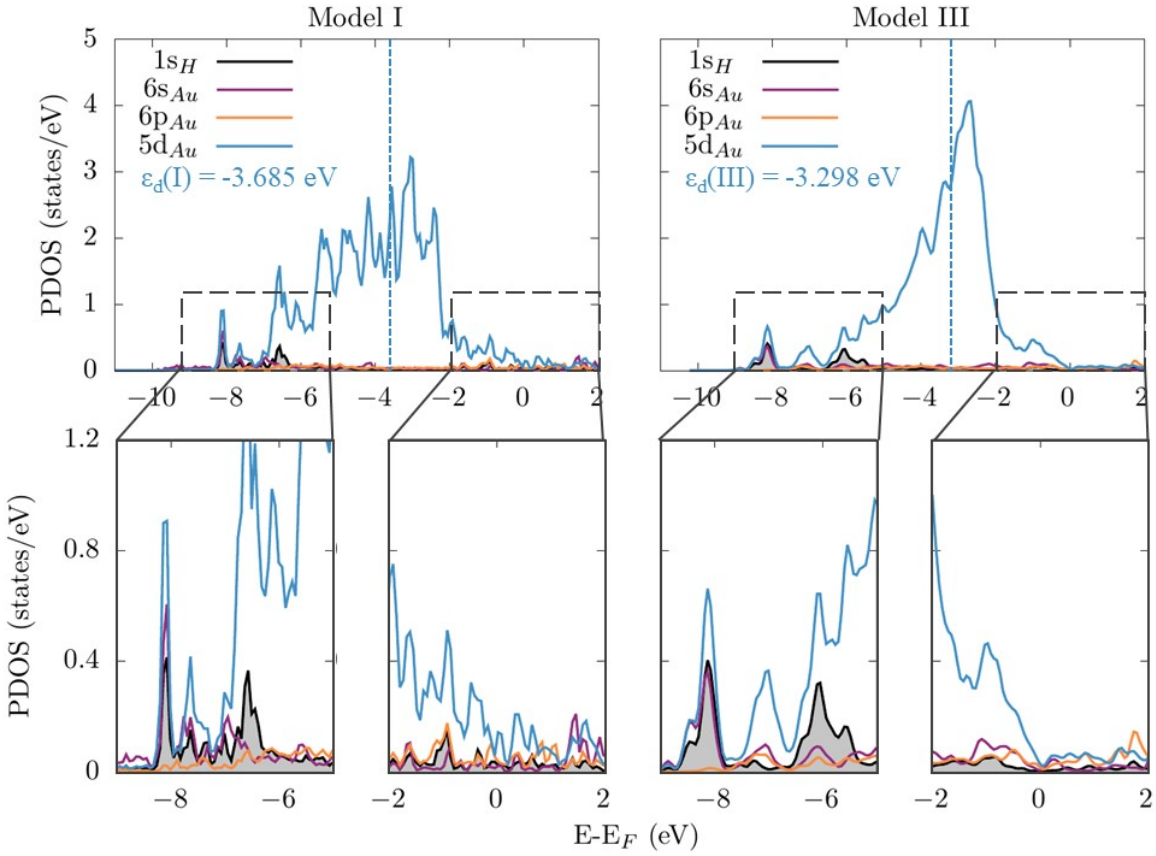

Figure SI.8: *Orbital-resolved projected density of states (PDOS) for H adsorbed on*

representative Au surface atoms in Model I (edge site) and Model III (chain site), with energies referenced to E_F.

Effect of full structural relaxation under hydrogen coverage through site-resolved Au PDOS (Fig. SI.9): Figure SI.9 reports site-resolved PDOSs for selected surface Au atoms TOh Model I (equivalent edge sites) and Model III (chain sites), comparing a rigid Au-lattice reference (left) with the fully optimized structure (right). In Model I, the local DOS is distributed over a broad energy window (≈5 eV) and the PDOS curves largely overlap, indicating a relatively homogeneous electronic response across the undercoordinated edge surface sites. Upon full structural optimization, the dominant Au manifold becomes noticeably narrower (≈3 eV) and develops a sharper, higher-intensity maximum, while site-to-site differences become more pronounced. This evolution is consistent with a relaxation-driven redistribution of local Au environments under hydrogen coverage (dynamic coordination and strain changes associated with reconstruction), which modifies the local spectral response without suppressing the finite DOS at the Fermi level.

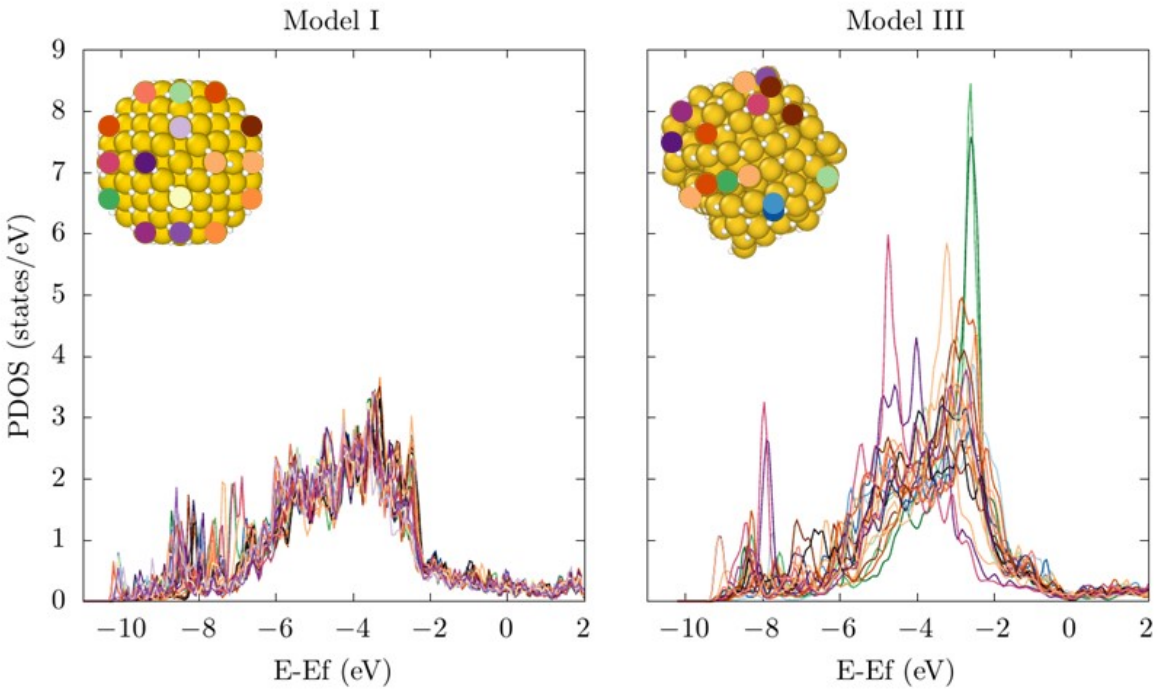

Figure SI.9: *Site-resolved Au projected density of states (PDOS) under hydrogen coverage for representative surface atoms in Model I (equivalent edge sites) and Model III (chain sites), with energies referenced to E_F. Left: rigid Au-lattice reference. Right: fully relaxed structure.*

Frontier response with Fukui analysis (Fig. SI.10): Fukui-function maps reported in Figure SI.10 show that hydrogen-driven reconstruction strongly redistributes the frontier response. In Model I, electron-accepting and electron-donating regions remain localized at pre-existing low-coordination vertices and edges, consistent with the classical undercoordination paradigm. In Model III, the frontier density spreads along the Au–H–Au network, indicating that the reconstructed surface behaves as an extended ensemble of electronically responsive chain sites rather than a sparse set of static hot spots. In other words, hydrogen-driven reconstruction converts a sparse set of static undercoordinated sites into an extended, electronically responsive chain ensemble.

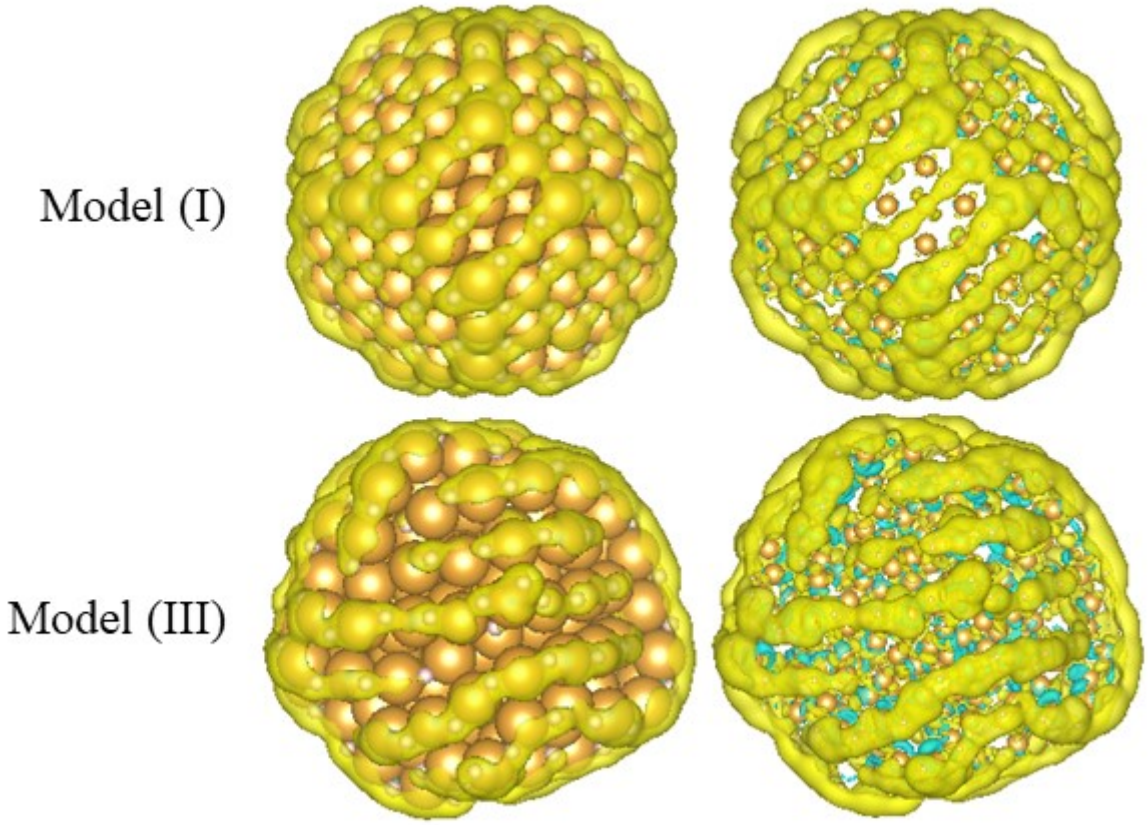

Figure SI.10: *Fukui-function maps illustrating the redistribution of frontier reactivity under hydrogen-driven reconstruction by adding 1 electron to the system. Top: Model I; bottom: Model III. Left panels: View of the Fukui function of the NP surface. Right panels: The atoms are shown smaller to visualise the electronic restructuring in the core of the NP.*

Ethene adsorption on chain versus edge ensembles and hydrogenation reaction (Fig. SI.11 and Table SI.2)

Ethene hydrogenation was examined on the hydrogenated TOh NP. Model I corresponds to the fixed-lattice reference (Au framework frozen) and the reaction is modeled at a representative undercoordinated edge Au–Au pair (see Fig. SI.11). Model III corresponds to the AIMD-derived, chain-rich reconstructed shell (300 K sampling followed by 0 K relaxation) and the reaction is modeled at a representative Au–H–Au chain segment.

To generate an adsorption site for C_2H_4 while maintaining a hydrogenated environment, one bridging H atom on the target Au–Au pair was removed. The local environment was then re-optimized using a constrained relaxation protocol: only the 6–8 nearest-neighbor Au atoms and their directly bound H atoms were allowed to relax, while all other atoms were kept fixed to their parent Model I or Model III coordinates. The local model and constrained region used in the present dataset are illustrated in Figure SI.11.

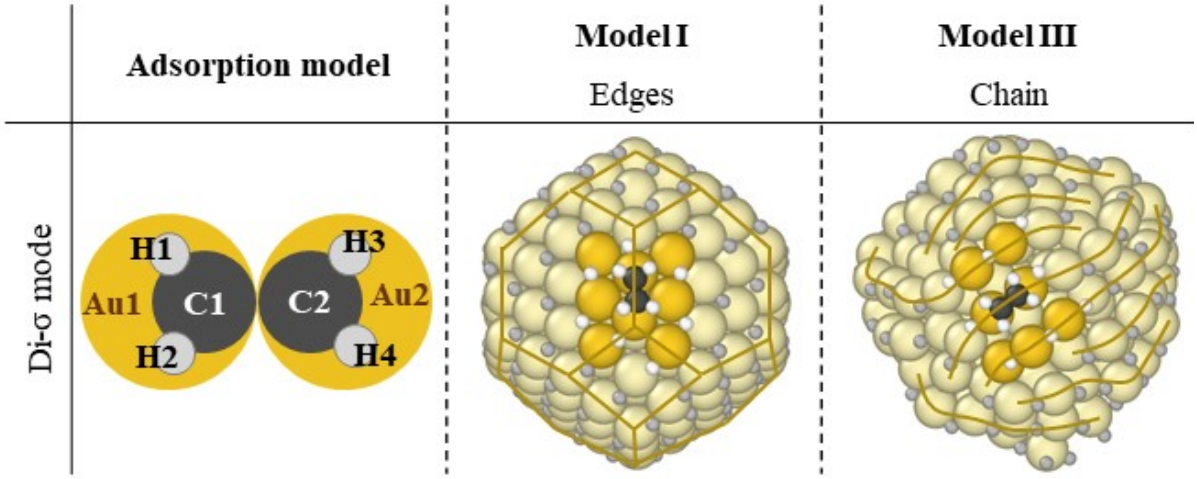

Figure SI.11: *Local model used for di-σ ethene adsorption and hydrogenation on representative Model I (edge) and Model III (chain) ensembles. Pale atoms indicate the constrained region; darker atoms indicate atoms allowed to relax during the local optimization steps.*

Entropic corrections were included for gas-phase species using tabulated thermochemical data (see Table SI.2). Adsorbed intermediates of hydrogenation reaction were treated within the frozen-surface approximation, neglecting translational and rotational entropy and without explicit vibrational free-energy corrections. Relative trends between models are therefore discussed at the level of electronic energies with gas-phase entropy corrections.

Table SI.2*: DFT electronic energies (E) and standard gas-phase entropies at 300 K for C_2H_4 and C_2H_6 used in free-energy corrections.*

	C_2H_4 (g)	C_2H_6 (g)
E (eV)	-31.88	-40.53
S (300 K) (eV/K)	$2.27e^{-3}$ [15]	$2.37e^{-3}$ [16]

Electronic Vibrational fingerprints and IR assignment (Table SI.3)

Early FTIR work on Au/CeO_2 reported a weak feature in the ~2125–2130 cm^{-1} region under H_2 [17], which was widely rationalized as a support-related electronic transition of Ce^{3+} (often described as a "forbidden" f–transition) rather than an Au–H vibration. In a key comparative FTIR study across oxides, Manzoli et al. (2012) [18] provided what they described as the first FTIR evidence of Au–H species, assigning a band at ~1620 cm^{-1} to an Au–H stretching mode on undercoordinated Au sites, and similarly assigning ~1621 cm^{-1} on Au/ZrO_2 to Au–H. In the same work, they also reported an additional band at ~1800 cm^{-1} on Au/CeO_2, tentatively attributed to Au–H and discussed as potentially sensitive to the charge state of Au clusters on reduced ceria. Importantly, Manzoli et al. still attributed the ~2126 cm^{-1} feature on Au/CeO_2 to the Ce^{3+} electronic transition (following earlier assignments), reinforcing the ambiguity of that spectral window. This interpretation was later challenged by Silverwood et al. (2016), who used H_2/D_2 reduction combined with inelastic neutron scattering (INS) to show that the ~2125–2130 cm^{-1} band cannot be purely a Ce^{3+} transition (its intensity changes upon isotopic substitution), supporting an Au–H contribution in that region. In this context, our AIMD-derived DFT results provide a unified structural origin for the coexistence of ~2100, ~1800, and ~1600 cm^{-1} signatures: they arise from distinct Au–H motifs (terminal/apical vs bridging in Au–H–Au chains vs more constrained chain-intersection environments), rather than a single "universal" Au–H frequency.

Table SI.3 specifies the different structural (local environment and Au-H bond length) and vibrational signatures at the molecular level depending on the types of hydrogen present on the NP after molecular dynamics. The results of this work are compared with those of other studies in the last column.

Table SI.3: *Calculated Au–H bond lengths and vibrational frequencies for distinct hydrogen motifs identified in the hydrogenated TOh NP (Model III), obtained from frequency calculations on AIMD-*

derived structures. Terminal (top/apical) and bridging Au–H environments within Au–H–Au chain motifs exhibit clearly differentiated stretching frequencies, spanning the ~2100, ~1800, and ~1600–1700 cm⁻¹ regions. The last column compares the computed spectral windows with reported FTIR/INS experimental assignments, highlighting that the debated ~2125–2130 cm⁻¹ band, as well as the ~1800 and ~1620 cm⁻¹ features observed on oxide-supported Au catalysts, can be rationalized by distinct local Au–H configurations rather than a single universal Au–H vibration.

This work: Frequency calculations on hydrogenated TOh NP (Model III)				Corresponding experimental window / literature context
Au–H motif	Local description	Au–H (Å)	ν(Au–H) (cm^{-1})	
H on top (terminal bonding)	2 H atoms bound to 1 Au in the chain Au-H-Au-H-Au	1.58 1.59	2160 2138	Falls in the debated ~2125–2130 region [17]
H on top (apical bonding)	Single H atom bounds to Au in the chain Au-H-Au-H-Au	1.59 1.60	2099 2017	High-frequency Au–H stretch (overlaps the "~2100" family) [19].
H on bridge	Au coordinated by 4 bridging H; one representative H reported	1.63	1785	Matches the ~1800 cm^{-1} band reported on Au/CeO_2 [18]
H on bridge	Chain Au with 2 bridging H + 1 apical H. Bridging H participating in chain motif	1.69 1.77	1680 1630	In the ~1600–1700 window; consistent with Au–H assignments around ~1620–1621 cm^{-1} on TiO2/ZrO_2 [18]

References

[1] K. P. Huber and G. Herzberg. Molecular Spectra and Molecular Structure. [Online; accessed 3. Feb. 2026].1979. doi: 10.1007/978-1-4757-0961-2.

[2] Min Yu and Dallas R. Trinkle. “Accurate and efficient algorithm for Bader charge integration”. In: J. Chem.Phys. 134.6 (Feb. 2011), p. 064111. issn: 0021-9606. doi:10.1063/1.3553716.

[3] A. D. Becke and K. E. Edgecombe. “A simple measure of electron localization in atomic and molecular systems”. In: J. Chem. Phys. 92.9 (May 1990), pp. 5397–5403.issn: 0021-9606. doi: 10.1063/1.458517.

[4] B. Silvi and A. Savin. “Classification of chemical bonds based on topological analysis of electron localization functions”. In: Nature 371 (Oct. 1994), pp. 683–686.issn: 1476-4687. doi: 10.1038/371683a0.

[5] J. Contreras-Garcıa and J. M. Recio. “Electron delocalization and bond formation under the ELF framework”. In: Theor. Chem. Acc. 128.4 (Mar. 2010), pp. 411–418.issn: 1432-881X. doi: 10.1007/s00214-010-0828-1.

[6] A. Otero-de-la-Roza, Erin R. Johnson, and Vıctor Luana. “Critic2: A program for real-space analysis of quantum chemical interactions in solids”. In: Comput.Phys. Commun. 185.3 (Mar. 2014), pp. 1007–1018. issn:0010-4655. doi: 10.1016/j.cpc.2013.10.026.

[7] Erin R. Johnson et al. “Revealing Noncovalent Interactions”. In: J. Am. Chem. Soc. 132.18 (May 2010), pp. 6498–6506. issn: 0002-7863. doi: 10.1021 /ja100936w.

[8] Julia Contreras-Garcıa et al. “NCIPLOT: a program for plotting non-covalent interaction regions”. In: J. Chem.Theory Comput. 7.3 (Mar. 2011), pp. 625–632. issn:1549-9626. doi: 10.1021/ct100641a. eprint: 21516178.

[9] Ruben Laplaza et al. “NCIPLOT and the analysis of noncovalent interactions using the reduced density gradient”. In: WIREs Comput. Mol. Sci. 11.2 (Mar. 2021), e1497. issn: 1759-0876. doi: 10.1002/wcms.1497.

[10] Yang, W.; Parr, R. G.; Pucci, R. Electron density, Kohn–Sham frontier orbitals, and Fukui functions. J. Chem. Phys. 1984, 81, 2862–2863.

[11] N.F. Barrera, J. Cabezas-Escares, F. Munoz, W.A. Muriel, T. Gomez, M. Calatayud, C. Cardenas, Fukui function and Fukui potential for solid-state chemistry: application to surface reactivity, J. Chem. Theory Comput. 21 (6) (2025) 3187–3203.

[12] Francesca Baletto and Riccardo Ferrando. "Structural properties of nanoclusters: Energetic, thermodynamic, and kinetic effects". In: Rev. Mod. Phys. 77.1 (May2005), pp. 371–423. doi: 10.1103/RevModPhys.77.371.

[13] Riccardo Ferrando, Julius Jellinek, and Roy L. Johnston. "Nanoalloys: From Theory to Applications of Alloy Clusters and Nanoparticles". In: Chem. Rev. 108.3 (Apr. 2008), pp. 845–910. issn: 0009-2665. doi: 10 .1021/cr040090g.

[14] Amanda S. Barnard et al. "Nanogold: A Quantitative Phase Map". In: ACS Nano 3.6 (June 2009), pp. 1431–1436. issn: 1936-0851. doi: 10.1021/nn900220k

[15] https://webbook.nist.gov/cgi/cbook.cgi?ID=C74851&Mask=7

[16] https://cccbdb.nist.gov/entropiesx.asp

[17] I. P. Silverwood et al. "Evidence for a surface gold hydride on a nanostructured gold catalyst". In: Chem.Commun. 52.3 (Dec. 2015), pp. 533–536. issn: 1359-7345. doi: 10.1039/C5CC06118K.

[18] Maela Manzoli et al. "Hydrogen interaction with gold nanoparticles and clusters supported on different oxides: A FTIR study". In: Catal. Today 181.1 (Feb. 2012), pp. 62–67. issn: 0920-5861. doi: 10.1016/j.cattod.2011.07.029.

[19] Xuefeng Wang and Lester Andrews. "Infrared Spectra and DFT Calculations for the Gold Hydrides AuH, (H2)AuH, and the AuH3 Transition State Stabilized in (H2)AuH3". In: J. Phys. Chem. A 106.15 (Apr.2002), pp. 3744–3748. issn: 1089-5639. doi: 10.1021/jp014105f.